Applied Catalysis B: Environmental 285 (2021) 119786

Contents lists available at ScienceDirect

Applied Catalysis B: Environmental

journal homepage: www.elsevier.com/locate/apcatb

Iron-modulated nickel cobalt phosphide embedded in carbon to boost power density of hybrid sodium–air battery

Yao Kang [a,1], Shuo Wang [a,1], Siqi Zhu [a,1], Haixing Gao [a], Kwan San Hui [b,*], Cheng-Zong Yuan [a], Hong Yin [a], Feng Bin [c], Xi-Lin Wu [d], Wenjie Mai [e], Ling Zhu [f], Maocong Hu [g], Feng Liang [h,*], Fuming Chen [i,*], Kwun Nam Hui [a,*]

[a] Joint Key Laboratory of the Ministry of Education, Institute of Applied Physics and Materials Engineering, University of Macau, Avenida da Universidade, Taipa, Macau SAR, 999078, China
[b] Engineering, Faculty of Science, University of East Anglia, Norwich, NR4 7TJ, United Kingdom
[c] State Key Laboratory of High-Temperature Gas Dynamics, Institute of Mechanics, Chinese Academy of Science, Beijing 100190, China
[d] College of Geography and Environmental Science, Zhejiang Normal University, Jinhua, 321004, China
[e] Siyuan Laboratory, Guangdong Provincial Engineering Technology Research Center of Vacuum Coating Technologies and New Energy Materials, Department of Physics, Jinan University, Guangzhou 510632, China
[f] College of Physics and Optoelectronics Engineering, Shenzhen University, Nanhai Ave, 3688, Shenzhen, Guangdong 518060, China
[g] Key Laboratory of Optoelectronic Chemical Materials and Devices, Ministry of Education, School of Chemical and Environmental Engineering, Jianghan University, Wuhan 430056, China
[h] State Key Laboratory of Complex Nonferrous Metal Resources Clean Utilization, Kunming University of Science and Technology, Kunming 650093, China
[i] Guangdong Provincial Key Laboratory of Quantum Engineering and Quantum Materials, School of Physics and Telecommunication Engineering, South China Normal University, Guangzhou 510006, China

ARTICLE INFO

Keywords:
Iron doping
Nickel cobalt phosphide
Electronic structure reformation
DFT calculation
Hybrid sodium-air battery

ABSTRACT

Nickel cobalt phosphide (NiCoP) is emerging as a potential electrocatalyst towards oxygen reduction reaction (ORR) and oxygen evolution reaction (OER). However, its ORR/OER activities are sluggish. Here, we investigated the roles of iron dopants in the Fe-doped NiCoP (Fe–NiCoP) in order to boost its ORR/OER kinetics. The density functional theory (DFT) calculations reveal that the Fe dopant effectively modulates the electron conductivity of NiCoP and reduces binding energies of the reaction intermediates towards rate-determining steps of ORR and OER. A binder-free 3D microflowers morphology of the Fe–NiCoP embedded in the amorphous carbon layer (Fe–NiCoP@C) catalyst on the nickel foam was prepared as the air cathode for the hybrid sodium-air battery (HSAB). The HSAB displays a discharge voltage of 2.74 V at 0.01 mA cm^{-2} with excellent round trip efficiency of 93.26 % at the 500th cycle and state-of-the-art power density of 621 mW g^{-1}.

1. Introduction

The rapid development of electric vehicles has stimulated the large demand for high-performance energy conversion and storage technologies, tackling the critical problems of climate change and energy crisis. Rechargeable metal − air batteries, especially, hybrid sodium-air batteries (HSABs) have attracted increasing attention due to their high theoretical energy density (2600 Wh kg^{-1}), natural abundance, and environmentally friendly characteristics [1–5]. In 2016, we are the first to show that the HSAB exhibits a large specific capacity of 835 mA h g^{-1} at 50 °C (corresponding to 99 % of the theoretical capacity) [2]. However, the practical application of HSABs has been largely obstructed by the four proton–electron transfer kinetics of oxygen reduction reaction (ORR) and oxygen evolution reaction (OER) due to the thermodynamically unfavorable process with large overpotential [1,6]. Although noble metals, such as platinum (Pt) and ruthenium (Ru) or iridium (Ir), have been commonly regarded as efficient electrocatalysts in ORR and OER, the high cost, scarcity, and poor chemical stability of these noble metal-based electrocatalysts have hindered their large-scale applications in HSABs [7,8]. Thus, the successful development of low-cost and highly efficient bifunctional electrocatalysts towards ORR and OER for HSABs has a significant impact on realizing the net-zero carbon society.

* Corresponding authors.
E-mail addresses: k.hui@uea.ac.uk (K.S. Hui), liangfeng@kust.edu.cn (F. Liang), fmchen@m.scnu.edu.cn (F. Chen), bizhui@um.edu.mo (K.N. Hui).
[1] These authors contributed equally.

https://doi.org/10.1016/j.apcatb.2020.119786
Received 28 July 2020; Received in revised form 31 October 2020; Accepted 17 November 2020
Available online 10 December 2020

Recently, transition metal phosphides (TMPs), such as Co_2P [9,10], CoP [11], Ni_2P [12], and MoP [13,14], have been recognized as promising alternatives to noble metal-free catalysts for the trifunctional electrocatalysts of ORR, OER, and hydrogen evolution reaction due to their multielectron orbitals, metallic characteristics, and low cost. Among these TMPs, NiCoP is particularly attractive because of two electrochemically feasible transition metals such as Ni and Co that contribute to the ORR and OER [15–18]. However, the critical problem of sluggish ORR/OER kinetics remains unaddressed, that is caused by the strong binding strength of the absorbed intermediates with the surface of Co and Ni atoms [15–18]. According to the Sabatier principle, the best catalysts should bond atoms or molecules with an intermediate strength: too weak interaction is not conducive to the activation of reactants, and too strong interaction is not beneficial for the desorption of products [19]. Therefore, there is a pressing need to improve our understanding of how to tune the adsorption/desorption strength of intermediates at the active sites of NiCoP, facilitating the ORR/OER kinetics and hence advancing metal-air batteries for large-scale applications.

In this study, through combined density functional theory (DFT) calculations and experimental investigations, we aim to understand the influence of Fe dopant in Fe-doped NiCoP (Fe-NiCoP) towards ORR/OER, in order to unveil its roles and the origin of improved ORR/OER activities. In addition, a layer of carbon coating is further coated onto the Fe–NiCoP surface (Fe–NiCoP@C) to facilitate the electron transport to and from the catalytic sites and further improve its catalytic performance and stability in the ORR and OER. The DFT calculations reveal that the Fe dopants in the Fe-NiCoP are the active sites for ORR/OER activities. The improved ORR/OER kinetics are facilitated by the enhanced electronic property of Fe–NiCoP@C and the reduced free energies of adsorption of oxygen-containing intermediates. The Fe–NiCoP@C catalyst exhibits excellent electrocatalytic performance toward ORR and OER with an onset potential of 0.81 V and exceptional overpotential of 340 mV at a current density of 50 mA cm^{-2}, which are higher than most of the non-noble metal-based ORR and OER catalysts reported to date. A HSAB, utilizing the binder-free 3D microflowers morphology of the Fe–NiCoP@C catalyst on the nickel foam as the air cathode, displays a discharge voltage of 2.74 V at 0.01 mA cm^{-2} with excellent round trip efficiency of 93.26 % at the 500th cycle and the state-of-the-art power density of 621 mW g^{-1}. The new understanding from this study helps to design new TMPs catalysts for advancements of metal-air batteries, realizing the potential of electric vehicles.

2. Experimental

2.1. Synthesis of Fe–NiCo LDH

The Fe-NiCo LDH were prepared by hydrothermal methods. Specifically, Nickle foam (NF) were cleaned with the assistance of sonication in HCl, ethanol, and water for 10 min each. Then, $Ni(NO_3)_2{\cdot}6H_2O$, $Fe(NO_3)_3{\cdot}9H_2O$, and $Co(NO_3)_2{\cdot}6H_2O$ (2:1:1) with 4 mmol NH_4F and 10 mmol urea were dissolved in 40 mL deionized (DI) water. Then, NF (2*3) and the solution were transferred into a 50 mL Teflon autoclave, sealed, and maintained at 120 °C for 9 h. The specific activity of the material for the target reaction is usually highly dependent on the chemical composition and their electronic structures. It has been demonstrated that Ni usually have a great influence on the OER activities, while Co and Fe ions are believed to be the active center towards ORR with specific crystal and electronic structures. To ensure the bifunctional catalytic performance of Fe-NiCoP for hybrid sodium-air battery, the ratio of Ni:Co and Ni:Co:Fe are about 1:1 and 1:0.5:0.5 for NiCoP and Fe-NiCoP, respectively.

2.2. Synthesis of Fe–NiCoP

To prepare the Fe–NiCoP@NF, the obtained Fe–NiCo LDH and 2 g $NaH_2PO_2{\cdot}H_2O$ were placed in two ceramic boats inside a tube furnace and annealed 300 °C for 2 h in a static N_2 atmosphere. Then, the samples were naturally cooled to room temperature in N_2 atmosphere.

2.3. Synthesis of Fe–NiCoP@C

The leaching of anions from TMP during oxidative reactions is still an important issue. Therefore, a layer of carbon was coated onto the Fe–NiCoP surface to stabilize the catalyst–electrolyte interface and provide additional direct electron transport paths. In the fabrication of carbon shell on the obtained Fe–NiCoP microflowers, the sample was transferred to a Teflon autoclave with 40 mL glucose solution (0.15 M) and then maintained at 180 °C for 4 h in an oven. Finally, the sample was carbonized at 400 °C for 2 h with an accelerating rate of 5 °C/min in N_2 atmosphere.

2.4. Electrochemical measurement

The electrochemical performance was carried out in a three-electrode setup with a CHI760e electrochemical station. Herein, Fe-NiCoP@C, Fe-NiCoP, NiCoP, commercial Pt/C, and Ir/C was utilized as the working electrode, Ag/AgCl and Pt foil was used as reference electrode and counter electrode, respectively. In this study, all potentials were calibrated to the reversible hydrogen electrode (RHE): $E_{RHE} = E_{measured} + 0.059*pH + 0.197$ V. The OER performance was tested in 1 M KOH without iR-correction. To investigate the ORR performance of materials, the active materials were peeled from the NF. 10 mg catalysts were added into 980 μl ethanol with 20 μl of 5 wt % Nafion solution to make catalyst ink. To prepare working electrode, 40 μl catalyst ink was dropped onto the surface of glass carbon electrode (diameter: 5 mm). The ORR performance of electrode was recorded in 0.1 M KOH at 1600 rmp with a sweep rate of 10 mV s^{-1}. All fresh electrolytes were bubbled with nitrogen for 30 min before test.

2.5. Assembly of the HSAB

The liquid anode was prepared by dissolving sodium metal into a solution of tetra ethylene glycol dimethyl ether. A piece of NASICON composed of $Na_3Zr_2Si_2PO_{12}$ with high ionic conductivity of 1.0×10^{-3} S cm^{-1} at room temperature was used as the separator [20,21]. The oxygen-saturated 0.1 M NaOH solution, which was used as the aqueous electrolyte, was sealed in a tube. A porous electrode containing 0.12 mg cm^{-2} catalyst was utilized as the air electrode. HSABs were assembled in a glove box filled with high-purity argon (O_2 and H_2O < 0.1 ppm) according to the following structure: liquid anode | NASICON | catholyte | catalytic cathode. The electrochemical performance of HSAB was tested at room temperature.

2.6. Material characterization

The crystallographic structure was determined using a Rigaku SmartLab XRD equipped with Cu Kα radiation (λ = ~1.54 Å), and the data were collected in the Bragg–Brentano mode with a scan rate of 5° s^{-1}. The morphology and structure were characterized using a Zeiss Sigma field emission scanning and Talos F200S transmission electron microscopes with an EDS probe. The surface chemical states were analyzed using a Thermo Scientific ESCALAB Xi^+ XPS Microprobe with Al–K_α radiation. ICP-AES (Thermo Jarrell Ash) was used to indicate the elemental composition of materials.

2.7. Computational details

All the calculations based on DFT were performed using the Vienna ab-initio Simulation Package in order to optimize the geometry structures and energies [22,23]. The exchange–correlation interactions of the generalized gradient approximation were determined in the scheme of

Perdew–Burke–Ernzerhof functional [24,25]. The core electrons was described using the Projector Augmented Wave (PAW) potential [26]. The cut-off kinetic energies in the plane waves were set to 450 eV for all the calculations. The convergence tolerance of energy and force on each atom during structure relaxation were less than 10^{-4} eV and 0.02 eV/Å, respectively. We build the 112 supercell of bulk Co_2P (a = b = 5.73 Å, c = 3.41 Å; α=β = 90°, γ = 120°) to dope Ni and Co atoms and ensure that the doping ratio is consistent with the experiment results (Fe:Co:Ni = 1:1:2 (at%)). Then, the cleave surface (111) of NiCoP and Fe-NiCoP are used for the subsequent adsorption calculation. The pseudo-potentials of Fe, Co and Ni metals all use the pseudo-potentials recommended by the VASP official website. We set the Brillouin zone with a Gamma-centered k-point grid of 5 × 5 × 1, and a vacuum space of around 20 Å was set along the z direction to avoid the interaction between periodical images [27]. Moreover, Grimme's DFT-D3 scheme was used to perform dispersion correction and describe the van der Waals (vdW) interactions in the systems [28,29]. The Hubbard-U correction method was applied to improve the descriptions of the strong localized Ni, Co, and Fe d-electrons in Fe–NiCoP with U = 5.3, U = 3.32 and U = 6.45 for Fe, Co, and Ni, respectively. These values were taken from previous studies. Spin polarization was also considered in all the calculations.

3. Results and discussion

3.1. Synthesis of Fe-NiCoP@C

The synthetic route of Fe–NiCoP@C composites is presented in Fig. 1a. Specifically, a hydrothermal method was initially applied, after which a yellow film was observed on the surface of the Ni foam, thus implying the successful formation of iron nickel cobalt layered double hydroxide (Fe–NiCo LDH) [30]. The obtained Fe–NiCo LDH precursor was subsequently converted to Fe–NiCoP via low-temperature phosphorization by using NaH_2PO_2 as the P source [31,32].

$$2NaH_2PO_2 \bullet H_2O \rightarrow PH_3 + Na_2HPO_4 + 2H_2O \quad (1)$$

$$NiCoFeO(OH) + PH_3 \rightarrow Fe\text{–}NiCoP + 2H_2O \quad (2)$$

After phosphorization, a carbon layer was coated onto the hierarchical Fe–NiCoP via hydrothermal carbonization of glucose [33]. During the process, glucose molecules were first cross-linked through the dehydration process to form an organic network surrounding the entire hierarchical Fe–NiCoP structure [33]. Finally, Fe–NiCoP@C was formed by annealing the cross-linked organic network at 400 °C for 2 h under an nitrogen atmosphere to form a carbonized layer with abundant oxygen functional groups [33].

3.2. Characterizations of materials

The X-ray diffraction (XRD) patterns of NiCoP, Fe–NiCoP, and Fe–NiCoP@C are shown in Fig. 1b. Compared to the XRD patterns of Fe–NiCo LDH (Fig. S1), the diffraction peaks at 41.0°, 47.6°, and 54.5° can be indexed to the (111), (210), and (211) crystal planes of NiCoP (JCPDS#71 – 2336), respectively, thereby indicating successful Fe incorporation without any phase change [34]. The scanning electron microscopy (SEM) results revealed that Fe–NiCo LDH, Fe–NiCoP, and Fe–NiCoP@C all exhibited a microflower-like morphology with the diameter ranging from 5 μm to 7 μm, as shown in Fig. 1c–e, indicating that the morphology was not influenced by phosphorization and carbonization. In addition, the enlarged SEM images (Fig. S2) showed that the surface of Fe–NiCoP was rough, suggesting that abundant active

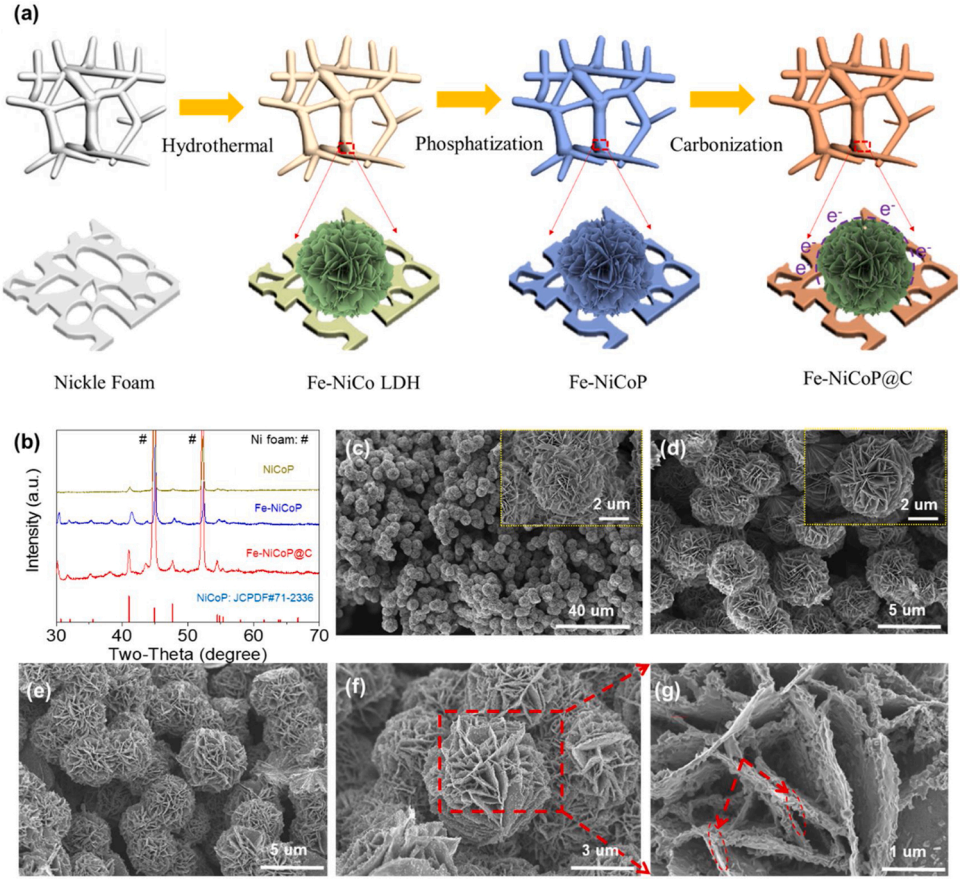

Fig. 1. (a) Schematic of the fabrication route of the hierarchical Fe–NiCoP@C and facile channels for electron transfer. (b) XRD patterns of NiCoP, Fe–NiCoP, and Fe–NiCoP@C. SEM images of (c) Fe–NiCo LDH, (d) Fe–NiCoP, and (e)–(g) Fe–NiCoP@C.

sites were generated after phosphorization. These bumps might be created due to the different inward and outward diffusion rates of P and OH^- during the phosphorization process [35]. The detailed SEM images shown in Fig. 1e−g and Fig. S2 showed that the Fe–NiCoP@C surface roughened considerably due to the integration of carbon networks in the Fe–NiCoP nanosheets. Firstly, the hierarchical carbon shell provides facile electron-transfer pathways between the active catalyst and the current collector. Secondly, the hierarchical structure also provides reactant/product exchange channels between neighboring chambers that are constructed by Fe-NiCoP@C nanosheet arrays. Transmission electron microscopy (TEM) was performed to gain further insights into the morphologies and sizes of the as-prepared materials. The Fe–NiCoP nanosheets clearly contained numerous bumps on the surface, which can provide extra electroactive sites and further boost their electrocatalytic performance (Fig. 2a and Fig. S3). As shown in Fig. 2b, the carbon layer with an approximate thickness of 5−15 nm was coated on the surface of Fe–NiCoP, and this coating was beneficial to the efficient electron transfer to and from the electroactive sites of the catalyst. The high-resolution TEM (HRTEM) images (Fig. 2c) of a single nanosheet of Fe–NiCoP@C demonstrated appropriately resolved lattice fringe spacings of 0.262 and 0.219 nm, corresponding to the (211) and (111) planes of NiCoP, respectively. This finding was also supported by several bright discrete spots in the selected area electron diffraction (SAED) pattern (insert of Fig. 2c), which could be indexed to the (111), (210), and (211) planes of NiCoP. Meanwhile, Fig. 2d−i show the high-angular annular dark field scanning TEM (HAADF − STEM); energy dispersive X-ray (EDX) mapping was then used to further investigate the element distribution of Fe–NiCoP@C. The EDX mapping in Fig. 2d−i indicated the almost homogeneous distributions of Ni, Co, Fe, P, and C except two rich signal of Ni in the EDX mapping, this may be attributed to the Ni region that connected Ni foam.

The surface chemical composition and atom valence states of NiCoP, Fe–NiCoP, and Fe–NiCoP@C were further examined by using X-ray photoelectron spectroscopy (XPS), as shown in Fig. 3. The XPS survey spectra identified the presence of Ni, Co, Fe, P, and C in the Fe–NiCoP@C electrode, suggesting the successful doping of Fe atoms and carbon coating. Specifically, the high-resolution XPS spectra of the Ni 2p, Co 2p, and Fe 2p regions of the catalysts were split into $2p_{3/2}$ and $2p_{1/2}$ doublets due to the spin–orbit coupling [36]. Fe–NiCoP@C exhibited five main peaks in the Ni 2p region. Two fitted peaks had binding energies of 856.2 (Ni $2p_{3/2}$) and 874.1 (Ni $2p_{1/2}$) eV, which are related to Ni $2p_{1/2}$ and Ni $2p_{3/2}$, whereas the peaks at 861.2 and 879.6 eV could be assigned to the satellite peaks of Ni 2p (Fig. 3a) [36–38]. Similarly, in the high-resolution Co 2p spectrum of Fe–NiCoP@C (Fig. 3b), the binding energies of 782.4 and 798.2 eV in the high-resolution Co 2p spectra were due to $2p_{3/2}$ and $2p_{1/2}$, whereas two peaks at 787.4 and 804.3 eV were assigned to the satellites of Co 2p, respectively [39,40]. Compared with NiCoP, the binding energies of Ni 2p and Co 2p in Fe–NiCoP and Fe–NiCoP@C shifted to higher binding energy, indicating electron transfer from Ni and Co to P atoms due to the incorporation of Fe, as discussed in the density functional theory (DFT). The high-resolution Fe 2p spectrum (Fig. 3c) showed four peaks divided into 712.1 eV of Fe $2p_{3/2}$ and 724.4 eV of Fe $2p_{1/2}$ with a spin − energy separation of 12.3 eV. The absence of characteristic FeP peaks in the Fe 2p region suggested the successful Fe doping in NiCoP [38]. As shown in Fig. 3d, the P 2p spectrum of Fe–NiCoP obtained a binding energy of 129.5 eV in $2p_{3/2}$, thereby indicating the presence of an M − P bond, whereas the centered peaks at 132.8 and 133.5 eV were assigned to the oxidized phosphorus species (M − PO) [41]. Compared with NiCoP, a negative shift simultaneously occurred in the P $2p_{3/2}$ binding energy (129.5 eV) of Fe–NiCoP and Fe–NiCoP@C, indicating an modification of the electronic structure upon incorporation of Fe atom, as discussed in the DFT [42]. In the high-resolution XPS spectrum of C 1s (Fig. S4), the binding energies of 283.4, 284.2, and 286.0 eV were assigned to the sp^2-hybridized carbon atoms (—CC), CC——═, and C(O)O, respectively [33]. Notably, the functionals groups, such as C—OC/COH, CO and C——═—OOH were

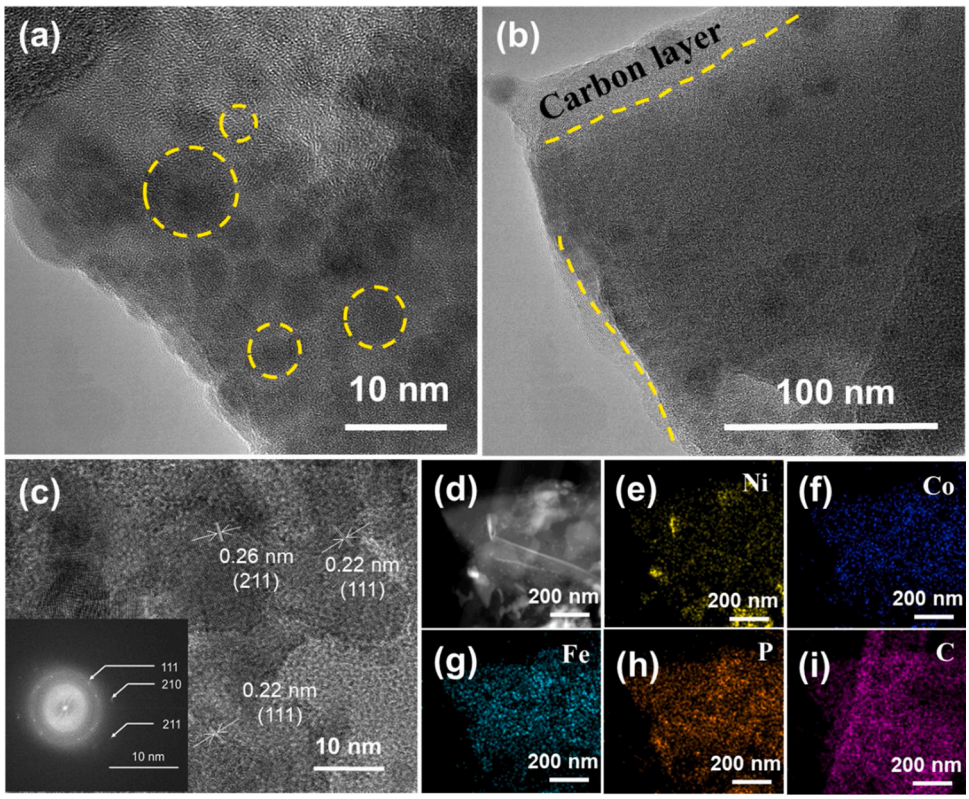

Fig. 2. (a)–(b) TEM images of Fe–NiCoP@C. (c) HRTEM images of Fe–NiCoP@C (insert is the SAED pattern of Fe–NiCoP@C). (d)−(i) EDX mapping of various elements in the porous Fe–NiCoP@C nanosheet.

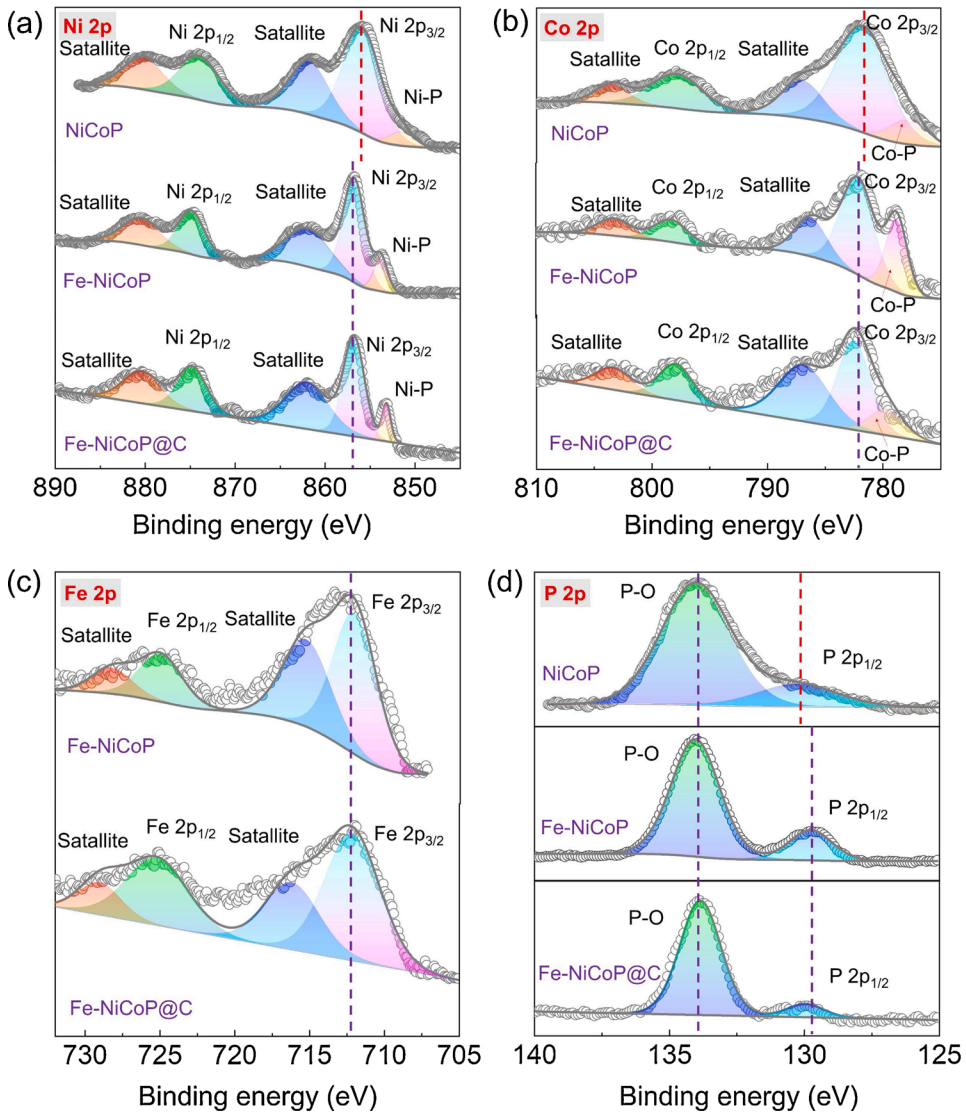

Fig. 3. XPS spectra of (a) Ni 2p, (b) Co 2p, (c) Fe 2p, and (d) P 2p of NiCoP (top), Fe–NiCoP (middle), and Fe–NiCoP@C (bottom), respectively.

observed in the C 1s. Such oxygen functional groups in carbonized layer facilitate the adsorption of water molecules via hydrogen bonding with oxygen functional groups [43]. In addition, these oxygen functional groups also provide additional active sites for ORR/OER activity by altering the electronic modulation of the adjacent carbon, which promotes the ORR/OER processes [44–46].

3.3. ORR and OER electrocatalysis

To evaluate the ORR performance of the as-prepared catalysts, rotating disk electrode measurements in O_2-saturated 0.1 M KOH were carried out. As indicated by the CV curves in Fig. 4a and Fig. S5, Fe–NiCoP@C displayed a reduction peak at the potential of 0.65 V, which is more positive than those of Fe–NiCoP (0.55 V), NiCoP (0.45 V), FeP@C (0.47 V), and Fe–NiP@C (0.45 V), suggesting the superior ORR catalytic performance of Fe–NiCoP@C. Meanwhile, the linear sweep voltammetry (LSV) was also investigated to reveal the ORR performance of the samples. Fig. 4b shows the LSV curves of Fe–NiCoP@C. Compared with Fe–NiCoP (0.80 V) and NiCoP (0.64 V), Fe–NiCoP@C obtained the maximum positive onset potential of 0.81 V. In addition, the larger limit current density of Fe–NiCoP and Fe–NiCoP@C indicated superior ORR performance compared with NiCoP. The LSV curves at different rotations were obtained to explore the electron transfer number (n) of air electrodes (Fig. 4c). The calculated n values of Fe–NiCoP@C, Fe–NiCoP, and NiCoP air electrodes were 3.75, 3.70, and 2.32, respectively. In the case of Fe–NiCoP@C, the calculated n value was almost similar to the $4e^-$ transfer number in the Pt/C. The ORR stability of Fe-NiCoP@C was also investigated in an O_2 saturated 0.1 KOH solution. The chronopotentiometry plots in Fig. S6 show the relative current remains 80 % after 10000 s, indicating acceptable stability of materials during the ORR test.

To investigate the effect of Fe incorporation and the coating of carbon layer on the OER catalytic activity of the Fe–NiCoP@C electrode, a series of electrochemical tests were carried out in 1 M KOH using the typical three-electrode system with a scan rate of 10 mV s^{-1} (Fig. 4d). Notably, Fe–NiCoP@C shows the best ORR activity, which need the lowest overpotential of 270 mV at the current density of 10 mA cm^{-2} compared to Fe–NiCoP (287 mV), NiCoP (319 mV), and Ir/C (350 mV). To achieve a higher current density of 50 mV cm^{-2}, Fe–NiCoP@C retained the lowest overpotential of 340 mV compared with Fe–NiCoP (370 mV), NiCoP (420 mV), and Ir/C (480 mV), revealing its high catalytic OER activities. The Tafel slopes (Fig. 4f) further revealed that Fe–NiCoP@C exhibited a smaller Tafel slope of 36 mV dec^{-1} than Ir/C (96 mV cm^{-1}), NiCoP (65 mV dec^{-1}), and Fe–NiCoP (62 mV dec^{-1}), signifying a superior OER performance of Fe–NiCoP@C. To further investigate the electrode reaction kinetics, electrochemical impedance

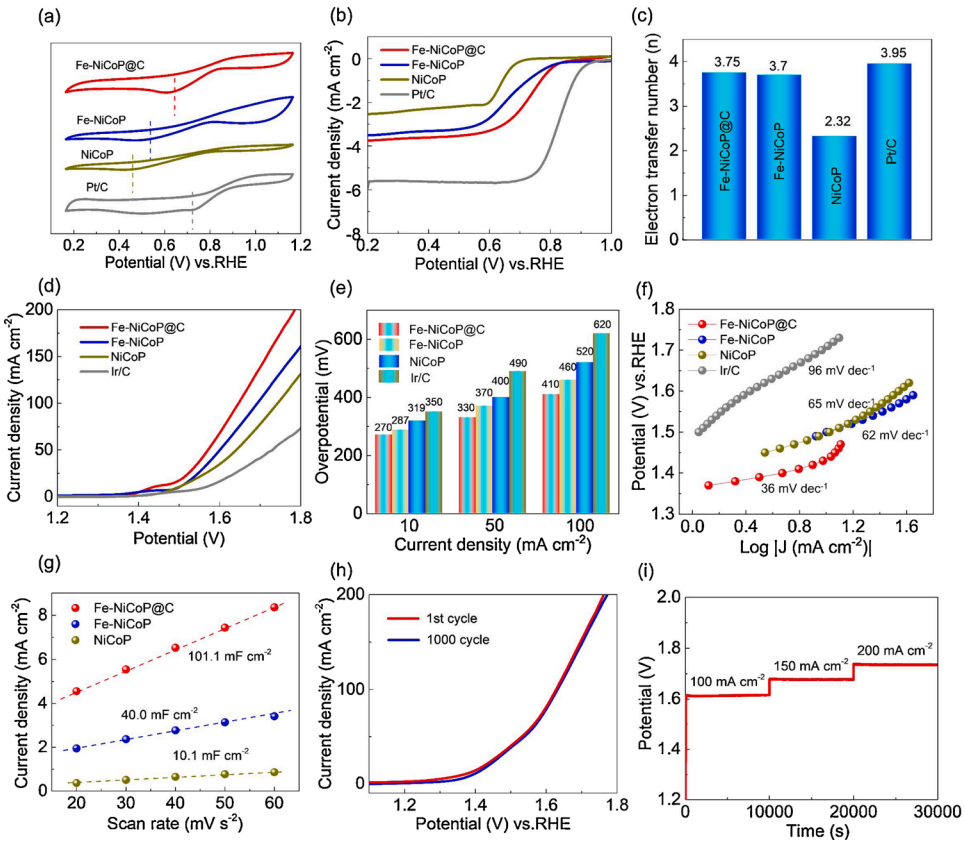

Fig. 4. (a) CV curves of NiCoP, Fe–NiCoP, Fe–NiCoP@C, and Pt/C in O_2-saturated 0.1 M KOH (1600 rpm, 10 mV s^{-1}). (b) ORR polarization curves of NiCoP, Fe–NiCoP, Fe–NiCoP@C, and Pt/C in O_2-saturated 0.1 M KOH (1600 rpm, 10 mV s^{-1}). (c) Electron transfer number of NiCoP, Fe–NiCoP, Fe–NiCoP@C, and Pt/C. (d) OER polarization curves of NiCoP, Fe–NiCoP, Fe–NiCoP@C, and Ir/C in 1 M KOH (1600 rpm, 10 mV s^{-1}). (e) Overpotentials of NiCoP, Fe–NiCoP, Fe–NiCoP@C, and Ir/C at the current density of 10, 50, and 100 mA cm^{-2} in 1 M KOH (10 mV s^{-1}). (f) Relevant Tafel plots of NiCoP, Fe–NiCoP, Fe–NiCoP@C, and Ir/C. (g) ECSA of NiCoP, Fe–NiCoP, and Fe–NiCoP@C. (h) LSV of Fe–NiCoP@C in the 1st and 1000th cycles. (i) Chronopotentiometry response of Fe–NiCoP@C at the constant current densities of 100, 150, and 200 mA cm^{-2}.

spectroscopy (EIS) was conducted. The equivalent circuit (inset of Fig. S7) comprised an electrolyte resistance (R_s) in series with a parallel combination of a constant phase element and a charge transfer resistance (R_{ct}). The Nyquist plot (Fig. S7) showed a smaller R_s of Fe–NiCoP@C (3.2 Ω) than those of Fe–NiCoP (3.5 Ω) and NiCoP (4.2 Ω), indicating that the Fe–NiCoP@C electrode possesses a low internal and interfacial resistances between the Fe–NiCoP@C surface and the electrolyte. Furthermore, Fe–NiCoP@C revealed a significantly smaller semicircle in the low-frequency region than the Fe–NiCoP and NiCoP electrodes, indicating its smaller charge transfer resistance and faster mass transfer kinetics during OER. Electrochemically active surface area (ECSA) is another important criterion for evaluating the active sites of catalysts wherein capacitance C_{dl} is determined via a simple CV test with different scan rates (10, 20, 30, 40, 50, and 60 mV s^{-1}). The CV curves of Fe–NiCoP and Fe–NiCoP@C (Fig. S8) and the calculated effective C_{dl} of ECSA (Fig. 4g) indicated that Fe–NiCoP@C possessed a significantly higher ECSA value of 100.1 m F cm^{-2} than Fe–NiCoP (40.0 m F cm^{-2}) and NiCoP (18.6 m F cm^{-2}). Thus, the incorporation of Fe and the coating of carbon layer led to the increase in abundant electroactive sites.

To evaluate the performance of electrocatalysts, electrochemical durability is carried out. The LSV curve of Fe–NiCoP@C remained nearly identical to the original curve after 1000 cycling tests (Fig. 4h), suggesting its excellent durability during cycling. To evaluate the durability of Fe–NiCoP@C, the long-term operation of the Fe–NiCoP@C sample was tested at 100, 150, and 200 mA cm^{-2} (Fig. 4i). The insignificant increase in measured potential indicated the good stability of Fe–NiCoP@C. The structural stability of Fe–NiCoP@C was also confirmed by the SEM results after long − term cycling test (Fig. S9). The SEM image of the cycled Fe–NiCoP@C revealed the good retention of porosity and uniformity in the microflowers. The observed stability can be partially attributed to the unique electrode structure, which provided good gas release ability and avoided the structural collapse caused by gas accumulation [33]. The robust mechanical strength between the as-grown catalysts and Ni foam substrates also contributed to the remarkable stability of Fe–NiCoP@C [33,47]. In addition, previous study has demonstrated that Fe-NiCoP would be oxidized during the process of OER, which also occurred in this work [34]. It is unavoidable to protect the oxidation process during OER even though carbon nanoflakes were utilized to protect the electrode. According to HRTEM results, the crystal lattices are disordered, implying that more and more amorphous structure of Fe-NiCoP have been formed along with the progress of OER. It is known that an amorphous structure has a lot of advantages to promote the process of OER. Furthermore, XPS was also tested to further explored the surface chemical composition and atom valence states after 1000 cycles of the OER test (Fig. S10). As show in the Fig. S10, the XPS survey spectra identified the presence of Ni, Co, Fe, P, O, and C in the Fe–NiCoP@C electrode. In particular, the Ni 2p spectrum shows that the Ni-P peak at a binding energy of 852.6 eV disappeared and the intensity of Ni-PO at about 856 eV was increased, indicating that the Ni-P on the surface of particles is oxidized. In the Co 2p region, the peaks for Co 2p after cycling are shifted toward lower binding energies compared with the original ones in Fe–NiCoP@C, which may imply the decrement of electron transfer, but it is not particularly noticeable. As for the Fe 2p, no significant change in the state of Fe atoms, suggesting that electrochemical test have not much influence on the Fe element. It is worth noting that the intensity of P 2p at about 129.9 eV was decreased and oxidized P species formed at about 134.4 eV, indicating the surface oxidation process occurred during the electrochemical test. In O 1s XPS spectrum, much oxygen element was observed after test, the fitted two peaks at 529.6 and 532.1 eV are ascribed to metal oxide (M-O), and metal oxyhydroxides (M-OH), respectively, which indicates that phosphides are slightly oxidized to phosphate, and the M-OH and M-O were gradually produced during the OER process, signifying the stability improvement [34]. These results revealed that Fe–NiCoP@C possessed significant durability in 1 M KOH.

To evaluate the catalytic properties of the Fe–NiCoP@C in real-life applications, the ORR and OER cycling performances of Fe–NiCoP@C was investigated using three electrodes in 0.1 M NaOH. No significant degradation was observed during all 45 cycles (Fig. S11). Furthermore, XRD was performed to investigate the chemical composition after cycling, and the results indicated the absence of an extra peak (Fig. S12) and the high structural stability of Fe–NiCoP@C during cycling. Notably, the majority of catalysts tend to experience severe erosion at high concentrations of the alkaline solution [33]. Therefore, the coating of the carbon layer on the Fe–NiCoP surface can provide effective protection against erosion and significantly improve the structural stability and cycling performance of the air electrode by reducing the leaching of P element during alkaline OER.

3.4. Mechanistic study on ORR and OER of materials

DFT calculations were performed to identify the origin of high catalytic performance and reveal the inherent relationship between the selective ORR/OER activity and atomic structure. To express the effect of doping clearly, the calculation model ignored the role of the outer carbon layer. Fig. S13a shows the top view of the (111) surface of the NiCoP structure, in which six-coordinated Co and the adjacent six-coordinated Ni atoms were exposed to the surface. In addition, the change of Bader charge between NiCoP and Fe-NiCoP (Table S3) indicates that the electrons transfer from Co and Ni atoms to neighbor P after the incorporation of Fe, which is consistent with XPS results and proves the rationality of the structure. Notably, the relatively lower *OH and O_2 adsorption energies in the Co active site (−0.14 and −1.34 eV) than those in the Ni site (0.46 and −0.46 eV) of NiCoP indicated the more favorable OER and ORR processes (Table S4). In the Fe–NiCoP structure (Fig. S13b), two different active sites, the Fe atom and its adjacent Ni atom, were considered in the simulation of the OER/ORR reaction due to the incorporation of Fe on the NiCoP surface. The slightly lower *OH and O_2 adsorption energies at the Fe site (−0.25 and −1.73 eV) compared with the values at the Ni-top site (0.46 and −0.42 eV) of Fe–NiCoP suggested that the Fe active sites were beneficial to OER and ORR. Therefore, the Co- and Fe-top sites were the active sites of the OER reaction before and after the incorporation of Fe, respectively.

The free energy pathways of the OER and ORR processes were also investigated through the simulation of the adsorption energies of intermediates, as shown in Fig. 5a–d. The adsorption behaviors of essential intermediates (including *OH, *O, and *OOH) during the OER process were investigated on the surface, implying that both the Co (NiCoP) and Fe (Fe–NiCoP) sites were stable in the adsorption of OER intermediates

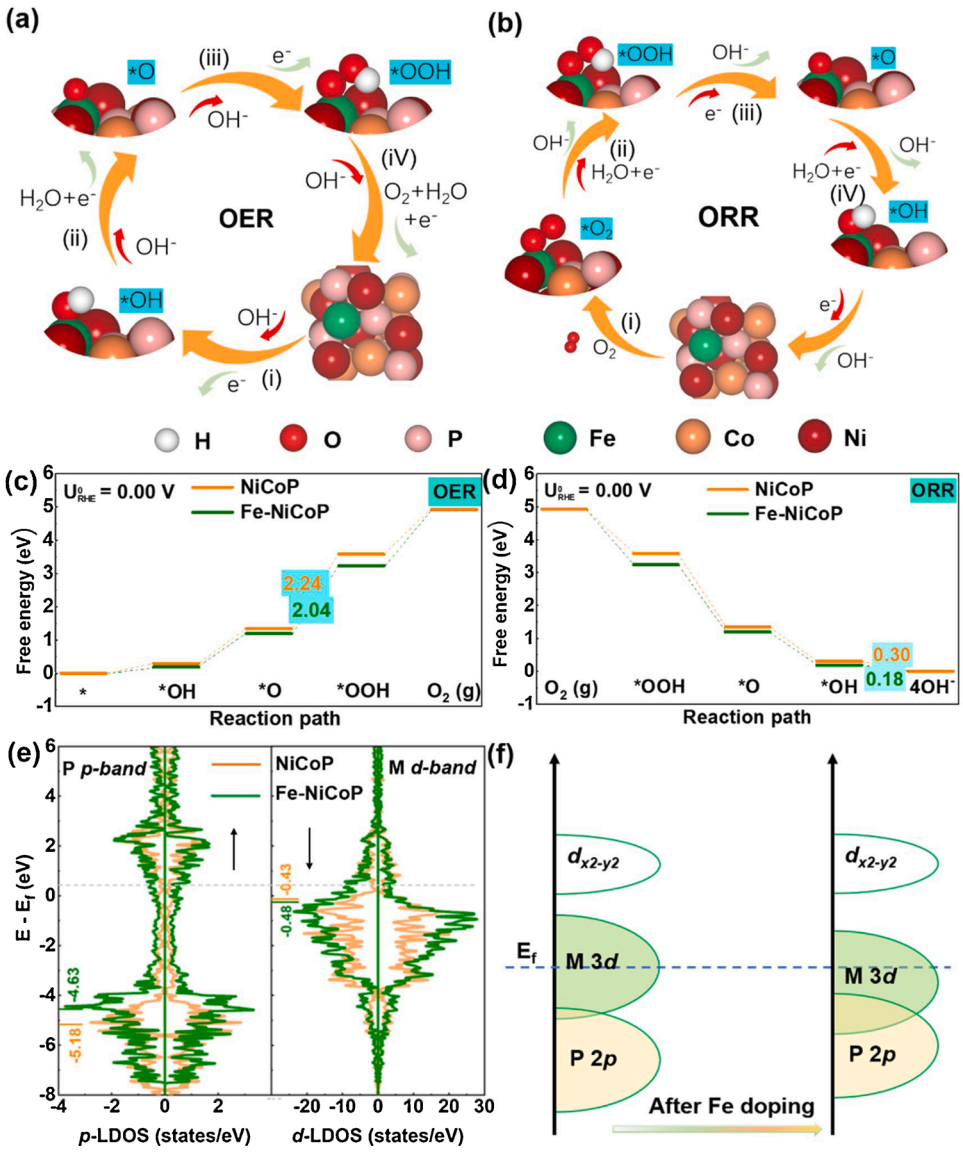

Fig. 5. Schematic of the *OH, *O, and *OOH intermediates in the Fe active sites of Fe–NiCoP for (a) OER and (b) ORR. The symmetric parts of the optimized slabs at the bottom excluded for clarity. (c)–(d) Calculated OER/ORR energy diagram of the NiCoP surface with (green line)/without (orange line) Fe doping. The green, orange, dark red, pink, red and white balls represent the Fe, Co, Ni, P, O and H atoms, respectively. The symmetric parts of the optimized slabs at the bottom are excluded for clarity. (e) p-band of P atoms related to OER and d-band of all the metal atoms related to ORR. (f) Schematic of the orbital changes in metal and nonmetal elements.

(Fig. 5a–b). Fig. 5c shows the diagram of OER Gibbs free energy (ΔG) in the (111) surface of NiCoP and Fe–NiCoP with correlative intermediates at the different reaction steps. The free energy profiles of NiCoP and Fe–NiCoP revealed how the OER rate-determining step (RDS) reflected the formation of *OOH. Moreover, the calculated corresponding theoretical overpotentials of 0.81 and 1.01 eV in Fe–NiCoP and NiCoP, respectively, suggested a favorable OER process in Fe–NiCoP. In the ORR process, the formation of the OH^- is the RDS (Fig. 5d). Furthermore, ΔG was calculated to be equivalent to an overpotential of 0.18 and 0.30 eV in Fe–NiCoP and NiCoP, respectively, suggesting that the Fe dopant could enhance the adsorption strength of the *OH and O_2 (g) intermediates on the surface of the NiCoP structure (Table S3), subsequently reducing the overpotential and promoting the ORR catalytic activity in the Fe–NiCoP catalyst.

To further understand the origin of the enhanced OER and ORR catalytic activities, the adsorption energies of *OH, *O, and *OOH in NiCoP and Fe–NiCoP were calculated. The lower adsorption energies of *OH, *O, and *OOH obtained in Fe–NiCoP (−0.25, 1.09, and 2.70 eV) compared with those of NiCoP (−0.14, 1.24, and 3.04 eV) (Table S4.) suggested the more favorable OER and ORR reactions in the Fe–doped NiCoP slab. Meanwhile, the adsorption energies of *OH, *O, and *OOH also provided insights into the distinct chemical adsorption characteristics of the Fe–NiCoP surface. The differences in charge density showed that electron transfers occurred between the interface of adsorbates (*OH, *OOH, *O) and the Fe–NiCoP substrate, which can be considered suitable adsorption sites for the intermediates (Fig. S14). The charge transfer from the substrate to the adsorbate might lead to effective molecule activation which, in turn, can promote the subsequent O_2 evolution [48]. Therefore, the decreased overpotential demonstrates that the OER and ORR activities in the catalysts are enhanced after the incorporation of Fe, and this finding is consistent with the experimental results.

To further understand the inherent electron variation in the enhanced catalytic performance upon Fe incorporation, the total and partial density of states (TDOS and PDOS) were calculated, as shown in Fig. S15. The TDOS and PDOS plots showed the valence bands of both the up- and downspin channels in NiCoP and Fe–NiCoP near the Fermi level and the metallic character of materials. Compared with NiCoP (Fig. S15), the relatively higher TDOS value of Fe–NiCoP at the Fermi level indicated the efficient modulation of electrical conductivity, which was induced by the Fe dopant atom. Furthermore, the corresponding *p*- and *d*-bands in OER and ORR were calculated to illustrate the electron-hybridized property of NiCoP and Fe–NiCoP (Fig. 5e). The *p*- and *d*-band centers are effective descriptors in evaluating the performance of OER and ORR, respectively [49–53]. Compared with NiCoP (−5.18 eV), the calculated P *p*-band centers of Fe–NiCoP (−4.63 eV) shifted toward the Fermi level, which increases the binding strength of *OH, *O, and *OOH on the surface sites and results in low reaction barrier of the RDS, thus improving OER performance. When the Fe atom was doped on the surface of NiCoP, the top valance band of Fe was able to efficiently transfer electrons to the P *p*-band of Fe–NiCoP, thus enhancing the M–P hybridization and OER performance [49]. In addition, previous studies have demonstrated that ORR activity is related to the *d*-band center of surface transition metals, which is correlated with the ability to form chemisorption bonds between oxygen intermediates and active sites [51,50–53]. Downshifting of the d-band center in Fe–NiCoP compared to that of NiCoP (Fig. 4e) indicates the presence of more antibonding state above the Fermi level, signifying the enhanced stability of the chemisorption bond between oxygen intermediates and active sites. Our results (Fig. 5f) showed that the *d*-band center of all the metal atoms (Fe, Co, Ni) in Fe–NiCoP was shifted away from the Fermi level than that of pristine NiCoP, indicating the enhanced electronic interaction between the metals and P, and thus increasing the bonding strength between active sites and the oxygen intermediates. Hence, the increased catalytic activity observed in the Fe–NiCoP can be associated with the modified electronic properties induced by the incorporation of Fe dopant in NiCoP.

3.5. Assembly of HSABs

To evaluate the catalytic properties of Fe–NiCoP@C in real applications, HSABs were assembled consisting of a liquid anode, a NASICON solid electrolyte ($Na_3Zr_2Si_2PO_{12}$), an aqueous catholyte, and an air electrode using Fe–NiCoP@C (Fig. 6a). During discharge, oxygen from the air diffused to the catalytic sites and then reduced to form OH^-. Meanwhile, in the anolyte, the liquid anode was oxidized and Na^+ was diffused with a NASICON solid electrolyte into the catholyte. Similarly, during the charge process, Na^+ in the catholyte was transferred back to the anolyte through the NASICON for electrodeposition on the anode. During the discharge–charge process, the reversible electrode and overall battery reactions occur as follows:

Anode: Na 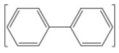 $\leftrightarrow Na^+ + e^-$ + 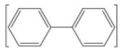

Cathode: $4OH^- \leftrightarrow 2H_2O + O_2 + 4e^-$

Overall: 4Na 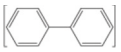 $+ 2H_2O + O_2 \leftrightarrow 4NaOH + 4$ 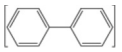

The electrochemical performance of fabricated HSABs was evaluated by examining their galvanostatic charge − discharge behaviors, as shown in Fig. 6b. In the figure, $\triangle V$ denotes the voltage gap between the charge and discharge voltages. The fabricated HSABs with Fe–NiCoP@C clearly showed the best battery performance with the lowest $\triangle V$ of 0.14 V at the current density of 0.01 mA cm^{-2}, followed by the Fe–NiCoP (0.3 V) and NiCoP (0.83 V). The initial round trip efficiencies (the charge-to-discharge voltage ratio) of the HSABs were 95.1 %, 90.1 %, and 74.7 % in Fe–NiCoP@C, Fe–NiCoP, and NiCoP, respectively. Fig. S16 shows the rate performance of HSAB with Fe–NiCoP@C electrode, an increased voltage gap was observed with increasing current density, which was attributed mainly to the high activation energy for the OER and ORR during battery operation at high current rates. Given that cycling performance and electrode stability are crucial to the air electrode in real applications, the constant current charge − discharge properties of HSABs were investigated for 500 cycles. Fig. 6c shows the charge–discharge profiles of HSABs with the Fe–NiCoP@C air electrode. Notably, a slight fluctuation in charging-discharging gap in the initial cycling process was observed, which is attributed to the surface reconstruction of materials, however, no significant decrease in potential can be observed under the continuous charge–discharge of batteries. To demonstrate the reversibility of the battery, the terminal discharge voltage and round trip efficiency of HSABs with the Fe–NiCoP@C electrode were measured (Fig. 6d). Notably, no significant degradation was observed after 500 cycles and the round trip efficiency remained at 93.26 %, thus revealing the high catalytic performance and excellent cycling performance of the Fe–NiCoP@C electrode. Compared with other reported materials in HSABs (Table S5), the remarkable fivefold enhancement in our results signified the excellence of our unique Fe–NiCoP@C electrode in real HSAB applications. The power density of HSABs with different air electrodes was also investigated, as shown in Fig. 6d. HSABs with the Fe–NiCoP@C air electrode obtained the highest power density of 621 mW g^{-1} compared with those with Fe–NiCoP (532 mW g^{-1}) and NiCoP (473 mW g^{-1}), thereby indicating the excellent ORR performance of the Fe–NiCoP@C air electrode. The capacities of the batteries were also investigated, as shown in Fig. S17. The battery with 1 M Na-BP-TEGDME displayed a capacity of around 15 Ah L^{-1}, which is comparable with the recently reported Na-aqueous-catholyte redox flow battery (17.3 Ah L^{-1}) [54].

4. Conclusion

In summary, we demonstrate a strategy to prepare binder-free 3D microflowers morphology of the Fe–NiCoP@C catalyst on the nickel foam as a highly efficient bifunctional air cathode for HSABs. The carbon layer effectively stabilizes the Fe–NiCoP electrolyte interface and

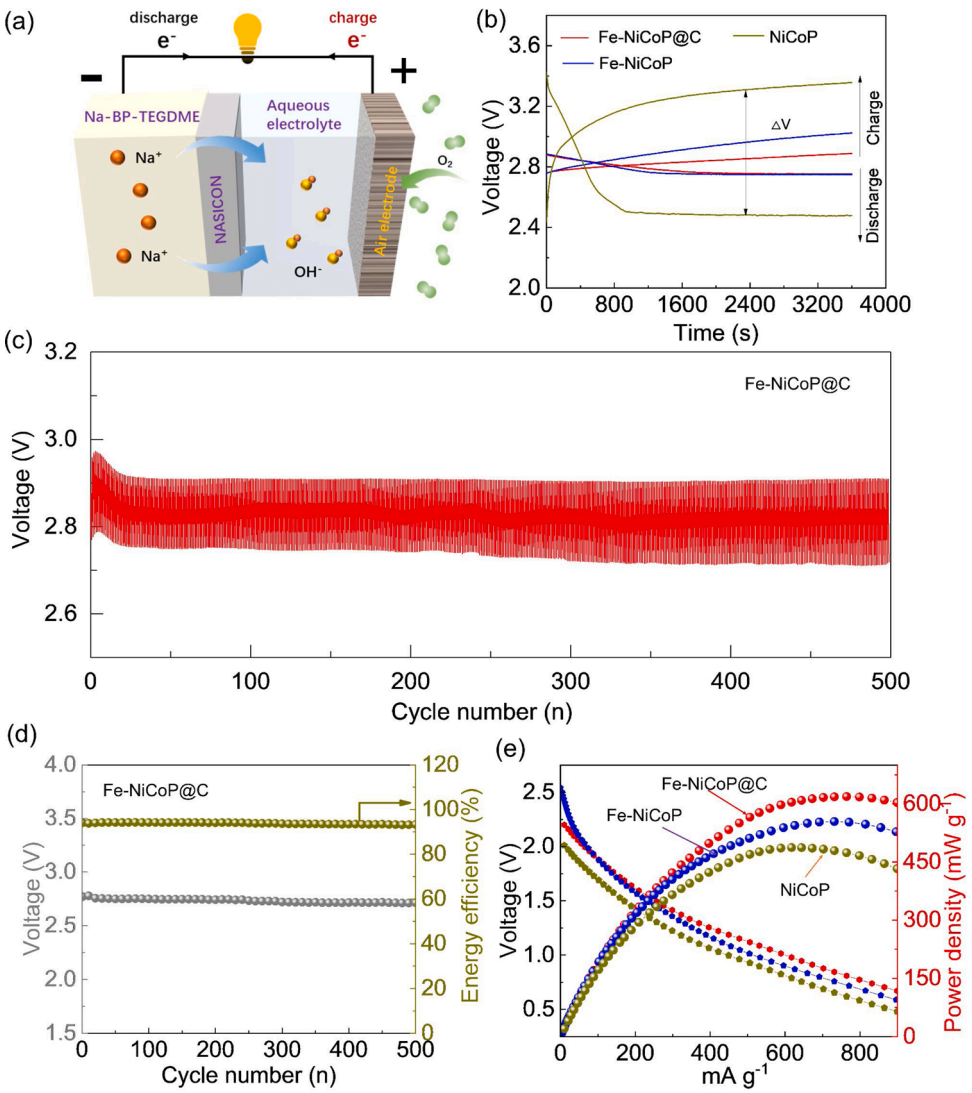

Fig. 6. (a) Schematic of HSAB. (b) Initial Charge – discharge voltage curves of the battery using different catalysts at a current density of 0.01 mA cm^{-2}. (c) Galvanostatic cycling of HSAB with Fe–NiCoP@C at a current density of 0.01 mA cm^{-2}. (d) Energy efficiency and cycling performance of battery with Fe–NiCoP@C at a current density of 0.01 mA cm^{-2}. (e) Power density of HSABs with NiCoP, Fe–NiCoP, and Fe–NiCoP@C.

improves the electron conduction and electrochemical activity. The DFT calculations reveal that the Fe dopant not only facilitates the electrical property of Fe–NiCoP but also performs as the active site for ORR/OER and reduces the free energies of adsorption of the oxygen-containing intermediates, thus leading to improved ORR and OER kinetics. This study sheds new light into the design and improvement of TMPs catalysts for ORR/OER and the new understanding can be applied to other fields in electrocatalysis.

CRediT authorship contribution statement

Yao Kang: Methodology, Investigation, Data curation, Writing - original draft. **Shuo Wang:** Writing - review & editing. **Siqi Zhu:** Data curation. **Haixing Gao:** Data curation. **Kwan San Hui:** Supervision, Conceptualization, Funding acquisition, Writing - review & editing. **Cheng-Zong Yuan:** Writing - review & editing. **Hong Yin:** Writing - review & editing. **Feng Bin:** Writing - review & editing. **Xi-Lin Wu:** Writing - review & editing. **Wenjie Mai:** Writing - review & editing. **Ling Zhu:** Writing - review & editing. **Maocong Hu:** Writing - review & editing. **Feng Liang:** Supervision, Writing - review & editing. **Fuming Chen:** Formal analysis, Funding acquisition, Writing - review & editing. **Kwun Nam Hui:** Supervision, Conceptualization, Funding acquisition, Writing - review & editing.

Declaration of Competing Interest

There are no conflicts to declare.

Acknowledgements

This work was funded by the Science and Technology Development Fund, Macau SAR (File no. 0191/2017/A3, 0041/2019/A1, 0046/2019/AFJ, 0021/2019/AIR), University of Macau (File no. MYRG2017-00216-FST and MYRG2018-00192-IAPME), the UEA funding, Zhejiang Province Basic Public Welfare Research Project (LGF19B070006), Science and Technology Program of Guangzhou (2019050001), and National Key Research and Development Program of China (2019YFE0198000). F. Chen acknowledges the Pearl River Talent Program (2019QN01L951). The DFT calculations were performed at High Performance Computing Cluster (HPCC) of Information and Communication Technology Office (ICTO) at University of Macau.

Appendix A. Supplementary data

Supplementary material related to this article can be found, in the online version, at doi:https://doi.org/10.1016/j.apcatb.2020.119786.

References

[1] Y. Kang, S. Wang, Y. Liu, K.S. Hui, H. Li, K.W. Ng, F. Liang, J. Geng, X. Hong, W. Zhou, K.N. Hui, Unveiling the Origin of Catalytic Sites of Pt Nanoparticles Decorated on Oxygen-Deficient Vanadium-Doped Cobalt Hydroxide Nanosheet for Hybrid Sodium–Air Batteries, ACS Appl. Energy Mater. 3 (2020) 7464–7473.

[2] Y. Kang, F. Liang, K. Hayashi, Hybrid sodium–air cell with Na[FSA–C2C1im][FSA] ionic liquid electrolyte, Electrochim. Acta 218 (2016) 119–124.

[3] F. Liang, X. Qiu, Q. Zhang, Y. Kang, A. Koo, K. Hayashi, K. Chen, D. Xue, K.N. Hui, H. Yadegari, X. Sun, A liquid anode for rechargeable sodium-air batteries with low voltage gap and high safety, Nano Energy 49 (2018) 574–579.

[4] X. Lin, Q. Sun, K. Doyle Davis, R. Li, X. Sun, The application of carbon materials in nonaqueous Na-O2 batteries, Carbon Energy 1 (2019) 141–164.

[5] H. Yadegari, X. Sun, Sodium–oxygen batteries: recent developments and remaining challenges, Trends Chem. 2 (2020) 241–253.

[6] Y. Kang, S. Wang, K. San Hui, H.-F. Li, F. Liang, X.-L. Wu, Q. Zhang, W. Zhou, L. Chen, F. Chen, K.N. Hui, [Fe(CN)6] vacancy-boosting oxygen evolution activity of Co-based prussian blue analogues for hybrid sodium-air battery, Mater. Today Energy (2020), 100572.

[7] B. Cai, R. Hübner, K. Sasaki, Y. Zhang, D. Su, C. Ziegler, M.B. Vukmirovic, B. Rellinghaus, R.R. Adzic, A. Eychmüller, Core–Shell structuring of pure metallic aerogels towards highly efficient platinum utilization for the oxygen reduction reaction, Angew. Chemie Int. Ed. 57 (2018) 2963–2966.

[8] J. Li, Z. Xi, Y.-T. Pan, J.S. Spendelow, P.N. Duchesne, D. Su, Q. Li, C. Yu, Z. Yin, B. Shen, Y.S. Kim, P. Zhang, S. Sun, Fe stabilization by intermetallic L10-FePt and Pt catalysis enhancement in L10-FePt/Pt nanoparticles for efficient oxygen reduction reaction in fuel cells, J. Am. Chem. Soc. 140 (2018) 2926–2932.

[9] Y. Guo, P. Yuan, J. Zhang, H. Xia, F. Cheng, M. Zhou, J. Li, Y. Qiao, S. Mu, Q. Xu, Co2P–CoN double active centers confined in n-doped carbon nanotube: heterostructural engineering for trifunctional catalysis toward HER, ORR, OER, and Zn–Air batteries driven water splitting, Adv. Funct. Mater. 28 (2018), 1805641.

[10] M. Song, Y. He, M. Zhang, X. Zheng, Y. Wang, J. Zhang, X. Han, C. Zhong, W. Hu, Y. Deng, Controllable synthesis of Co2P nanorods as high-efficiency bifunctional electrocatalyst for overall water splitting, J. Power Sources 402 (2018) 345–352.

[11] T. Liu, P. Li, N. Yao, G. Cheng, S. Chen, W. Luo, Y. Yin, CoP-doped MOF-based electrocatalyst for pH-universal hydrogen evolution reaction, Angew. Chemie 131 (2019) 4727–4732.

[12] Y. Li, H. Zhang, M. Jiang, Q. Zhang, P. He, X. Sun, 3D Self-supported Fe-doped Ni2P nanosheet arrays as bifunctional catalysts for overall water splitting, Adv. Funct. Mater. 27 (2017), 1702513.

[13] Y. Jiang, Y. Lu, J. Lin, X. Wang, Z. Shen, A hierarchical MoP nanoflake array supported on Ni Foam: a bifunctional electrocatalyst for overall water splitting, Small Methods 2 (2018), 1700369.

[14] X. Zhang, X. Yu, L. Zhang, F. Zhou, Y. Liang, R. Wang, Molybdenum phosphide/carbon nanotube hybrids as ph-universal electrocatalysts for hydrogen evolution reaction, Adv. Funct. Mater. 28 (2018), 1706523.

[15] S. Surendran, S. Shanmugapriya, A. Sivanantham, S. Shanmugam, R. Kalai Selvan, Electrospun Carbon Nanofibers Encapsulated with NiCoP: A Multifunctional Electrode for Supercapattery and Oxygen Reduction, Oxygen Evolution, and Hydrogen Evolution Reactions, Adv. Energy Mater. 8 (2018), 1800555.

[16] H. Zhang, X. Li, A. Hähnel, V. Naumann, C. Lin, S. Azimi, S.L. Schweizer, A. W. Maijenburg, R.B. Wehrspohn, Bifunctional Heterostructure Assembly of NiFe LDH Nanosheets on NiCoP Nanowires for Highly Efficient and Stable Overall Water Splitting, Adv. Funct. Mater. 28 (2018), 1706847.

[17] C. Liu, G. Zhang, L. Yu, J. Qu, H. Liu, Oxygen Doping to Optimize Atomic Hydrogen Binding Energy on NiCoP for Highly Efficient Hydrogen Evolution, Small 14 (2018), 1800421.

[18] M. Kong, Z. Wang, W. Wang, M. Ma, D. Liu, S. Hao, R. Kong, G. Du, A.M. Asiri, Y. Yao, X. Sun, NiCoP Nanoarray: A Superior Pseudocapacitor Electrode with High Areal Capacitance, Chem. Eur. J. 23 (2017) 4435–4441.

[19] Y. Sun, L. Yuan, Z. Liu, Q. Wang, K. Huang, S. Feng, Optimization of oxygen evolution dynamics on RuO2via controlling of spontaneous dissociation equilibrium, Mater. Chem. Front. 3 (2019) 1779–1785.

[20] M. Hou, F. Liang, K. Chen, Y. Dai, D. Xue, Challenges and perspectives of NASICON-type solid electrolytes for all-solid-state lithium batteries, Nanotechnology 31 (2020), 132003.

[21] C. Xu, K. Zhang, D. Zhang, S. Chang, F. Liang, P. Yan, Y. Yao, T. Qu, J. Zhan, W. Ma, B. Yang, Y. Dai, X. Sun, Reversible hybrid sodium-CO2 batteries with low charging voltage and long-life, Nano Energy 68 (2020), 104318.

[22] S. Grimme, Semiempirical GGA-type density functional constructed with a long-range dispersion correction, J. Comput. Chem. 27 (2006) 1787–1799.

[23] G. Kresse, J. Furthmuller, Efficient iterative schemes for ab initio total-energy calculations using a plane-wave basis set, Phys. Rev. B 54 (1996) 11169–11186.

[24] J.P. Perdew, K. Burke, M. Ernzerhof, Generalized gradient approximation made simple, Phys. Rev. Lett. 77 (1996) 3865–3868.

[25] J.P. Perdew, Y. Wang, Pair-distribution function and its coupling-constant average for the spin-polarized electron gas, Phys. Rev. B 46 (1992) 12947–12954.

[26] P.E. Blöchl, Projector augmented-wave method, Phys. Rev. B 50 (1994) 17953–17979.

[27] H.J. Monkhorst, J.D. Pack, Special points for Brillouin-zone integrations, Phys. Rev. B 13 (1976) 5188–5192.

[28] S. Grimme, J. Antony, S. Ehrlich, H. Krieg, A consistent and accurate ab initio parametrization of density functional dispersion correction (DFT-D) for the 94 elements H-Pu, J. Chem. Phys. 132 (2010), 154104.

[29] S. Grimme, S. Ehrlich, L. Goerigk, Effect of the damping function in dispersion corrected density functional theory, J. Comput. Chem. 32 (2011) 1456–1465.

[30] Q. Yang, T. Li, Z. Lu, X. Sun, J. Liu, Hierarchical construction of an ultrathin layered double hydroxide nanoarray for highly-efficient oxygen evolution reaction, Nanoscale 6 (2014) 11789–11794.

[31] P. Xiao, W. Chen, X. Wang, A review of phosphide-based materials for electrocatalytic hydrogen evolution, Adv. Energy Mater. 5 (2015), 1500985.

[32] C. Xuan, J. Wang, W. Xia, Z. Peng, Z. Wu, W. Lei, K. Xia, H.L. Xin, D. Wang, Porous Structured Ni–Fe–P Nanocubes Derived from a Prussian Blue Analogue as an Electrocatalyst for Efficient Overall Water Splitting, ACS Appl. Mater. Interfaces 9 (2017) 26134–26142.

[33] B. Zhang, Y.H. Lui, A.P.S. Gaur, B. Chen, X. Tang, Z. Qi, S. Hu, Hierarchical FeNiP@Ultrathin Carbon Nanoflakes as Alkaline Oxygen Evolution and Acidic Hydrogen Evolution Catalyst for Efficient Water Electrolysis and Organic Decomposition, ACS Appl. Mater. Interfaces 10 (2018) 8739–8748.

[34] Q. Zhang, D. Yan, Z. Nie, X. Qiu, S. Wang, J. Yuan, D. Su, G. Wang, Z. Wu, Iron-Doped NiCoP Porous Nanosheet Arrays as a Highly Efficient Electrocatalyst for Oxygen Evolution Reaction, ACS Appl. Energy Mater. 1 (2018) 571–579.

[35] T. Zhai, L. Wan, S. Sun, Q. Chen, J. Sun, Q. Xia, H. Xia, Phosphate Ion Functionalized Co3O4 Ultrathin Nanosheets with Greatly Improved Surface Reactivity for High Performance Pseudocapacitors, Adv. Mater. 29 (2017), 1604167.

[36] Y. Wu, X. Tao, Y. Qing, H. Xu, F. Yang, S. Luo, C. Tian, M. Liu, X. Lu, Cr-Doped FeNi–P Nanoparticles Encapsulated into N-Doped Carbon Nanotube as a Robust Bifunctional Catalyst for Efficient Overall Water Splitting, Adv. Mater. 31 (2019), 1900178.

[37] V.H. Hoa, D.T. Tran, H.T. Le, N.H. Kim, J.H. Lee, Hierarchically porous nickel–cobalt phosphide nanoneedle arrays loaded micro-carbon spheres as an advanced electrocatalyst for overall water splitting application, Appl. Catal. B Environ. 253 (2019) 235–245.

[38] T. Wu, S. Sun, J. Song, S. Xi, Y. Du, B. Chen, W.A. Sasangka, H. Liao, C.L. Gan, G. G. Scherer, L. Zeng, H. Wang, H. Li, A. Grimaud, Z.J. Xu, Iron-facilitated dynamic active-site generation on spinel CoAl2O4 with self-termination of surface reconstruction for water oxidation, Nat. Catal. 2 (2019) 763–772.

[39] G. Zhang, B. Wang, J. Bi, D. Fang, S. Yang, Constructing ultrathin CoP nanomeshes by Er-doping for highly efficient bifunctional electrocatalysts for overall water splitting, J. Mater. Chem. A 7 (2019) 5769–5778.

[40] Y. Li, B. Jia, B. Chen, Q. Liu, M. Cai, Z. Xue, Y. Fan, H.-P. Wang, C.-Y. Su, G. Li, MOF-derived Mn doped porous CoP nanosheets as efficient and stable bifunctional electrocatalysts for water splitting, Dalton Trans. 47 (2018) 14679–14685.

[41] H. Li, Q. Li, P. Wen, T.B. Williams, S. Adhikari, C. Dun, C. Lu, D. Itanze, L. Jiang, D. L. Carroll, G.L. Donati, P.M. Lundin, Y. Qiu, S.M. Geyer, Colloidal Cobalt Phosphide Nanocrystals as Trifunctional Electrocatalysts for Overall Water Splitting Powered by a Zinc–Air Battery, Adv. Mater. 30 (2018), 1705796.

[42] Z. Xiao, Y. Wang, Y.-C. Huang, Z. Wei, C.-L. Dong, J. Ma, S. Shen, Y. Li, S. Wang, Filling the oxygen vacancies in Co3O4 with phosphorus: an ultra-efficient electrocatalyst for overall water splitting, Energy Environ. Sci. 10 (2017) 2563–2569.

[43] S.T. Senthilkumar, S.O. Park, J. Kim, S.M. Hwang, S.K. Kwak, Y. Kim, Seawater battery performance enhancement enabled by a defect/edge-rich, oxygen self-doped porous carbon electrocatalyst, J. Mater. Chem. A 5 (2017) 14174–14181.

[44] D. Yan, Y. Li, J. Huo, R. Chen, L. Dai, S. Wang, Defect chemistry of nonprecious-metal electrocatalysts for oxygen reactions, Adv. Mater. 29 (2017), 1606459.

[45] S. Chen, J. Duan, M. Jaroniec, S.-Z. Qiao, Nitrogen and oxygen dual-doped carbon hydrogel film as a substrate-free electrode for highly efficient oxygen evolution reaction, Adv. Mater. 26 (2014) 2925–2930.

[46] Y. Zhai, Z. Zhu, S. Dong, Carbon-based nanostructures for advanced catalysis, ChemCatChem 7 (2015) 2806–2815.

[47] P. Wang, Z. Pu, Y. Li, L. Wu, Z. Tu, M. Jiang, Z. Kou, I.S. Amiinu, S. Mu, Iron-Doped Nickel Phosphide Nanosheet Arrays: An Efficient Bifunctional Electrocatalyst for Water Splitting, ACS Appl. Mater. Interfaces 9 (2017) 26001–26007.

[48] L. Cai, B. Qiu, Z. Lin, Y. Wang, S. Ma, M. Wang, Y.H. Tsang, Y. Chai, Active site engineering of Fe- and Ni-sites for highly efficient electrochemical overall water splitting, J. Mater. Chem. A 6 (2018) 21445–21451.

[49] A. Grimaud, K.J. May, C.E. Carlton, Y.-L. Lee, M. Risch, W.T. Hong, J. Zhou, Y. Shao-Horn, Double perovskites as a family of highly active catalysts for oxygen evolution in alkaline solution, Nat. Commun. 4 (2013) 2439.

[50] Y. Tian, S. Wang, E. Velasco, Y. Yang, L. Cao, L. Zhang, X. Li, Y. Lin, Q. Zhang, L. Chen, A Co-Doped Nanorod-like RuO2 Electrocatalyst with Abundant Oxygen Vacancies for Acidic Water Oxidation, iScience 23 (2020), 100756.

[51] F. Ando, T. Tanabe, T. Gunji, S. Kaneko, T. Takeda, T. Ohsaka, F. Matsumoto, Effect of the d-Band Center on the Oxygen Reduction Reaction Activity of Electrochemically Dealloyed Ordered Intermetallic Platinum–Lead (PtPb) Nanoparticles Supported on TiO2-Deposited Cup-Stacked Carbon Nanotubes, ACS Appl. Nano Mater. 1 (2018) 2844–2850.

[52] F.H.B. Lima, J. Zhang, M.H. Shao, K. Sasaki, M.B. Vukmirovic, E.A. Ticianelli, R. R. Adzic, Catalytic activity−d-Band center correlation for the O2 reduction reaction on platinum in alkaline solutions, J. Phys. Chem. C 111 (2007) 404–410.
[53] X. Tian, X. Zhao, Y.-Q. Su, L. Wang, H. Wang, D. Dang, B. Chi, H. Liu, E.J. M. Hensen, X.W. Lou, B.Y. Xia, Engineering bunched Pt-Ni alloy nanocages for efficient oxygen reduction in practical fuel cells, Science 366 (2019) 850.
[54] S.T. Senthilkumar, J. Han, J. Park, S. Min Hwang, D. Jeon, Y. Kim, Energy efficient Na-aqueous-catholyte redox flow battery, Energy Storage Mater. 12 (2018) 324–330.